Acta Geotechnica
https://doi.org/10.1007/s11440-023-02019-8

RESEARCH PAPER

# Behaviour of bio-inspired grouped battered minipiles under lateral loading in clay

Sanchari Mondal[1] · Mahdi M. Disfani[1] · Amirhassan Mehdizadeh[1]

Received: 16 October 2022 / Accepted: 13 July 2023


**Abstract**
The field of bio-inspired geotechnics has been growing in response to the demand for foundations that are sustainable and yet have improved load-bearing capacities. This study aims to address the gap in a specialised adaptation of root system architecture for designing resilient foundations. The lateral load behaviour of one such novel grouped battered minipile configuration is evaluated in this study based on full-scale field testing and numerical modelling to report the unknown increase of load capacity caused by shape modification. First, three single minipiles battered at 0° and 25° were subjected to static lateral loading in fine-grained soil. The strain profiles along the individual minipile shafts were obtained using optic fibre sensors. Consecutively, full-scale lateral load tests on two types of minipile groups were also performed; one group had a configuration of two 25° battered minipiles perpendicular to the direction of loading mimicking a tree-root system, and another conventional group had two positive and negative battered minipiles. A numerical model was developed to investigate the effect of pile spacing and obtain soil pressures, bending moments and axial forces of the battered minipile groups. Results show that increased bearing area and higher engagement of soil volume for the novel minipile group with two perpendicular battered minipiles were larger than the conventional minipile group; thus, the former offered higher lateral resistance. The deflection pattern, bending moment and *p-y* curves showed a shadowing effect in stiff clay for battered minipile groups at a pile head spacing of three times the minipile diameter.

**Keywords** Battered minipile group · Bio-inspired · Finite difference method · Lateral load · Optic fibre

## 1 Introduction

In the domain of foundation engineering, bio-inspired geotechnics can be implemented to improve design for increased capacity and sustainability; and tree root system architecture is one such possible source of inspiration for the same. One of the leading areas of bio-inspired geotechnics is root-inspired anchorage systems and the load transfer mechanism between these foundations and soil [34]. The design of such foundations is inspired by the biological strategies that the roots of trees represent in nature. The process of translating bio-inspired geotechnics to foundation engineering is demonstrated in Lu and Mitchell [32] by Jason T. DeJong. It begins with testing a root system, followed by the comparison of their load–displacement plots, then converting the 3D imaging of the root system into a 3D model and ultimately, assessing its load capacity by adopting physical/full-scale modelling. The past tree-root anchor research has focused on overturning and pullout modes of failure [12, 33]. According to Burrall et al., [12] in comparison to conventional shallow footings, the root systems can display as high as 100 times higher efficiency. It has been reported by Frost et al., [20] that when a branching angle of 15° and 30° is adopted, it increases the downward bearing capacity by two and three times, respectively, in comparison to the traditional vertical piles. Additionally, it was reported by Jewell and Wroth [26] that a reinforcement battered at 60° with respect to the opposite direction of shear loading (30° batter angle with respect to the vertical axis) gives maximum shear resistance. Thus, in order to adopt the root-inspired anchorage systems, it is essential that the load transfer mechanism of

✉ Mahdi M. Disfani
mmiri@unimelb.edu.au

[1] Department of Infrastructure Engineering, Faculty of Engineering and Information Technology, The University of Melbourne, Block B 207, Melbourne, VIC 3010, Australia

Published online: 11 August 2023

these systems is well understood through field and laboratory testing and numerical modelling. Although various aspects of root systems, such as soil exploration, anchorage, and transport, can be adopted for inspiration, this study only hinges on the increased bearing area (or volume) of root systems.

Mostly, the root networks of the plants provide anchorage only up to shallow depths subjected to lower confining stress [34]. Hence, adopting their design strategies could be most appropriate for designing micropile or minipile groups. The theory of micropiling was first introduced by Dr. Lizzi in 1952 when he patented the 'root pile', which is essentially a network of reticulated piles analogous to a tree root network [31]. Similar to micropiles, minipiles are hollow small-diameter piles, with a typical diameter of 42.4 mm and length of up to 2 m, that are generally driven into the soil in battered (reticulated) configuration and usually in groups. Hence, these minipile groups are designed to resist uplift, compressive and lateral loading. The advantages of quick installation and increased load-bearing capacity compared to typical shallow foundations have made these systems very popular in Australia and globally for supporting light structures and infrastructures. They can be used to retrofit existing foundations in areas with difficult or remote access, mimicking the root grafting strategy. Minipiles are physically similar to conventional battered micropiles and are installed without grouting, with minimal disturbance to the surrounding soil and structures. Micropiles, monopiles and piles, in general, have a wide range of applications in resisting lateral loads from superstructures such as transmission towers, offshore structures, solar panels and highway gantries etc., in both clay and sand [25]. Although minipiles differ from micropiles regarding the installation procedure and absence of grouting, previous studies on micropiles are often referred to for designing minipiles, as both have overlapping characteristics such as diameter, length and load-bearing mechanism. Abd Elaziz and El Naggar [2] performed field experimentation and numerical modelling on vertically installed hollow-bar micropiles in clay. Their analysis showed that a plastic hinge occurs for the micropiles at a depth of seven to ten times the micropile diameter under lateral load in very stiff clay.

Piles can be installed at batter angles when the lateral load on a vertical pile exceeds the allowable limit [39, 46], which is also applicable for micropiles [28]. The design of vertical micropiles subjected to lateral loading is similar to that used for piles [1]. The performance of single battered piles in sand as a function of the length-to-diameter ratio and the relative density of the soil was studied by Sharma and Hussain [57] and Zhang et al. [62], respectively. They reported optimum batter angles under lateral load for various length-to-diameter ratios and relative density of sand. Empirical correlations to predict the lateral load capacity of single battered micropiles were also proposed by Kyung and Lee [28]; however, they were based on limited physical and field experiments in cohesionless soil only. Rao and Veeresh [51] performed lateral load tests on model minipiles battered at two angles (positive and negative 30°) in clay. They reported that the higher lateral capacity of the negative batter pile (loading in the direction opposite of batter) can be attributed to higher passive pressure developed for the negative battered piles, in comparison to positively battered and vertically installed piles. The number of experimental studies reported on full-scale battered piles in clay is very limited, with no information on strain profile and bending; hence, the soil-pile interaction of battered piles in cohesive soil is not well understood. Thus, before evaluating the behaviour of branched minipile groups, the first objective was to obtain force–displacement curves and strain profiles of single minipiles by performing full-scale field experimentation under lateral loading.

A categorisation of root systems based on five types of branching patterns, such as VH-type, V-type, H-type, M-type and R-type, was proposed by Yen [60]. VH-type root structure has horizontal and vertical roots, H-type and V-type belong to horizontal and vertical roots, respectively; M-type roots grow in various directions, while R-type root structure is dominant with inclined roots. The R-type root architecture was reported to offer the highest shear resistance in soil by Fan and Chen [18]. The battered pile groups are more representative of tree root networks extending in the soil with an inclination angle. Conventional battered pile group configurations are commonly used as foundations of structures such as bridge piers due to their greater lateral resistance compared to vertically installed pile groups [37]. The spacing between the piles, the fixity at the pile cap, and the orientation of the pile group relative to the loading direction are some of the factors that impact the efficiency of pile groups. Among the previous studies on pile groups, Brown et al., [10] observed the shadowing effect based on tests performed on hollow steel piles with a spacing of three times the diameter ($3B$) of the pile in dense sand. To account for the overlapping shear zones, $p$-multipliers were also proposed. In clay, however, this effect was reportedly lower, as observed by Brown and Reese [11]. Vertical pile groups were also studied by Morrison and Reese [43] in clay and by Rollins et al., [56] in the sand with a similar spacing pattern, where the leading piles carried more load than their trailing counterparts. As the spacing increased from 3 to $5B$ in loose and medium-dense sand, very little change occurred in $p$-multipliers [38]. According to Kim and Yoon [27], spacing larger than $6B$ in loose and medium-dense sand and $8B$ for dense sand caused no group effect, and for clay,

this value was found to be 5*B*–6*B* [49]. The diminishing shadowing effect as the spacing increased from 3 to 7*B* was also reported by Chandrasekaran et al., [13] in soft clay. They looked into the pile head fixity as well and found that partial fixity causes a maximum bending moment to occur at a larger depth compared to fixed-headed piles. McVay et al., [37] also studied pile head fixity for vertical piles as well as battered piles and concluded that the maximum bending occurs at the pile head in a fixed-head group. However, only conventional battered pile group configurations were considered. Abu-Farsakh et al., [3] performed a numerical analysis of three pile groups, vertical, battered, and mixed (both vertical and battered), with the same spacing. They reported that battered pile groups have a higher lateral load resistance compared to mixed and vertical pile groups, which matches the observation by Zhang et al., [61]. It can be deduced from the literature that both batter angle and pile head spacing are important parameters influencing the lateral resistance of a pile group.

The studies summarised above concern mainly the vertically installed pile groups—there is limited literature available on the performance of battered micropile groups in clay. Also, limited battered pile group configurations have been studied previously, only involving conventional positive and negative battered piles in the trailing and leading row [3, 61]. Full-scale lateral load tests on pile groups with more than 5*B* spacing are also very limited [13]. Thus, the second objective of this study is to investigate the performance of battered minipile groups from a soil-structure interaction perspective; hence, full-scale minipile group systems with different configurations in clay were tested. The tests also introduce a new battered minipile group configuration which is a simplified physical adaptation of the root network with an asymmetric orientation and branching angle.

## 2 Experimental procedures

### 2.1 Subsurface soil properties

The test site was located in Dookie, a town in the Goulburn Valley region of Victoria, Australia. The local hills in the Dookie region are mainly comprised of alluvium, Cambrian and Ordovician rocks. The quaternary sediment is made of Colluvium, which is aprons of gravel and clay. The rocks of the Dookie hills comprise rocks of the Mount Wellington Fault Zone, a geological feature that cross-cuts Victoria [17].

The in situ testing included seven cone penetration tests (CPT) around the site performed mainly to check the uniformity of the clay site and to assist in identifying the most suitable locations for testing. The test site map and the location of the boreholes for the seven CPT tests are shown in Fig. 1, along with the test locations. Three of the CPT results nearest to the location of the lateral loading tests are presented in Fig. 2a, b. The site investigation performed showed that the sub-surface soil condition consisted of mainly medium stiff clay and no water table down to the depth of penetration. The soil can be categorised as clay to silty clay with intermittent zones of clayey silt from the soil behaviour type (SBT) classification chart by Robertson [54] based on cone resistance and normalised friction ratio. Also, Dynamic Cone Penetration tests (DCP) per AS 1289.6.3.2 [5] (Fig. 2c) were conducted up to a depth of 1 m and 1.3 m for single and group minipiles, respectively, adjacent to each test location.

The soil unit weight ($\Upsilon$) was approximated to range from 18.6 kN/m$^3$ to 19.0 kN/m$^3$ from the CPT results [55] using the relation,

$$\Upsilon = \left(0.27\left(\log R_f\right) + 0.36[\log(q_t/P_a)] + 1.236\right)\Upsilon_w \qquad (1)$$

where $R_f$ is the friction ratio, $q_t$ is corrected cone resistance, $P_a$ is atmospheric pressure, and $\Upsilon_w$ is the unit weight of water. The average modulus of elasticity of the soil was estimated to be 14 MPa equivalent to $\alpha(q_t\text{-}\sigma_{vo})$ where $\alpha$ is the modulus factor, and $q_t\text{-}\sigma_{vo}$ is the net cone resistance [55] up to 1.6 m of depth from the cone penetration tests (Fig. 2a, b). The DCP penetration index in mm/blow values was used to calculate CBR (California Bearing Ratio), and CBR was further used to estimate the values of undrained shear strength $S_u$ using the equation $S_u = (CBR/0.56)^{0.935}$ [15]. The correlation from the DCP results adjacent to each test gave an undrained shear strength, $S_u$, ranging from 36 to 40 kPa for the testing location of single piles, and 52 and 45 kPa for the testing location of the first and second groups of minipiles, respectively. These values were consistent with the overall undrained shear strength obtained from CPT; however, DCP results were chosen as they were performed adjacent to each test location. The liquid limit and plastic limit of the soil at 1 m depth were 53 and 21, respectively, and the soil can be classified as highly plastic clay (CH) with a plasticity index of 32 based on the Unified Soil Classification System.

### 2.2 Test minipiles

The full-scale test minipiles were 1.6 m long hollow pipes with an external diameter of 42.4 mm and a thickness of 2.5 mm, made of stainless steel with a modulus of elasticity of $2 \times 10^5$ MPa. The relative stiffness of the piles can be determined using Eq. 2, proposed by Poulos and Davis [47].

$$K_{rs} = E_p I_p / E_h L^4 \qquad (2)$$

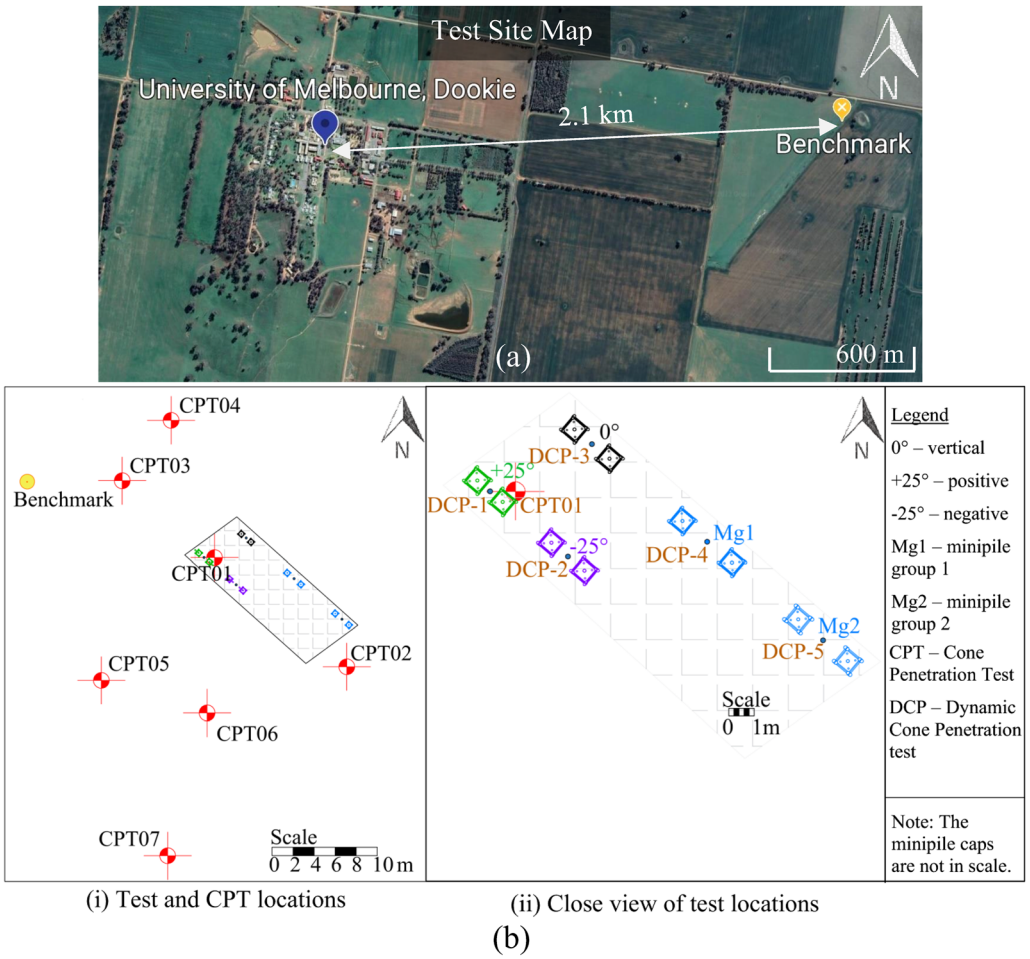


**Fig. 1** **a** Test site map, **b** test and CPT locations, and **c** close view of test locations

where $E_pI_p$ is the flexural rigidity of the pile, $E_h$ is the horizontal soil modulus of elasticity at the pile tip calculated using Vesic [58]'s formula and $L$ is the embedded length of the pile. When the relative stiffness of the pile, $K_{rs}$, determined by Eq. 2, is less than $10^{-2}$, the pile can be considered flexible [40]. $K_{rs}$ was calculated to be $1.8 \times 10^{-3}$ for an embedment length of 1.27 m, the flexural rigidity of $2.5 \times 10^4$ N m$^2$ and $E_h$ of 5.5 MPa; hence, the minipiles in this study are considered flexible similar to that of the biological materials.

## 2.3 Optic fibre instrumentation

Fibre Bragg grating (FBG) based optic fibre sensors were used to monitor strain on piles by Lee et al. [29], Doherty et al. [16], and Li et al. [30], among others. They are preferred over conventional electric strain gauges owing to their ease of installation, lighter weight, smaller physical dimensions, longevity and resistance to electromagnetic interference [24]. The working principle of the FBGs is based on Bragg's law developed by W.H. Bragg and W.L. Bragg [30]. The incident broadband light on the optic fibre is reflected by the Bragg grating, whose periodic modulation matches the central wavelength of the light [24]. When the optic fibre is subjected to strain and temperature change, it is reflected in a shift of central wavelength. The relation between the central Bragg wavelength and the strain under constant temperature [45] is shown in Eq. 3.

$$\frac{\Delta\lambda_B}{\lambda_B} = \left(1 - p_{eff}\right)\Delta\varepsilon \tag{3}$$

where $\Delta\lambda_B$ denotes the shift in central Bragg wavelength, $p_{eff}$ is the photo-elastic parameter, and $\Delta\varepsilon$ is the strain. Thus, the strain or temperature change can be obtained from the shift in wavelength.

The FBG sensors are generally installed in grooves in the minipile shaft using a two-part epoxy and allowed to cure for the bond to gain strength [16, 30]. The minipiles in this study were instrumented with optic fibres using a similar technique. 1.5 mm deep, 4 mm wide and 1.35 m long groove was machined on each of the minipiles, and an optic fibre with six FBGs was laid in the groove and

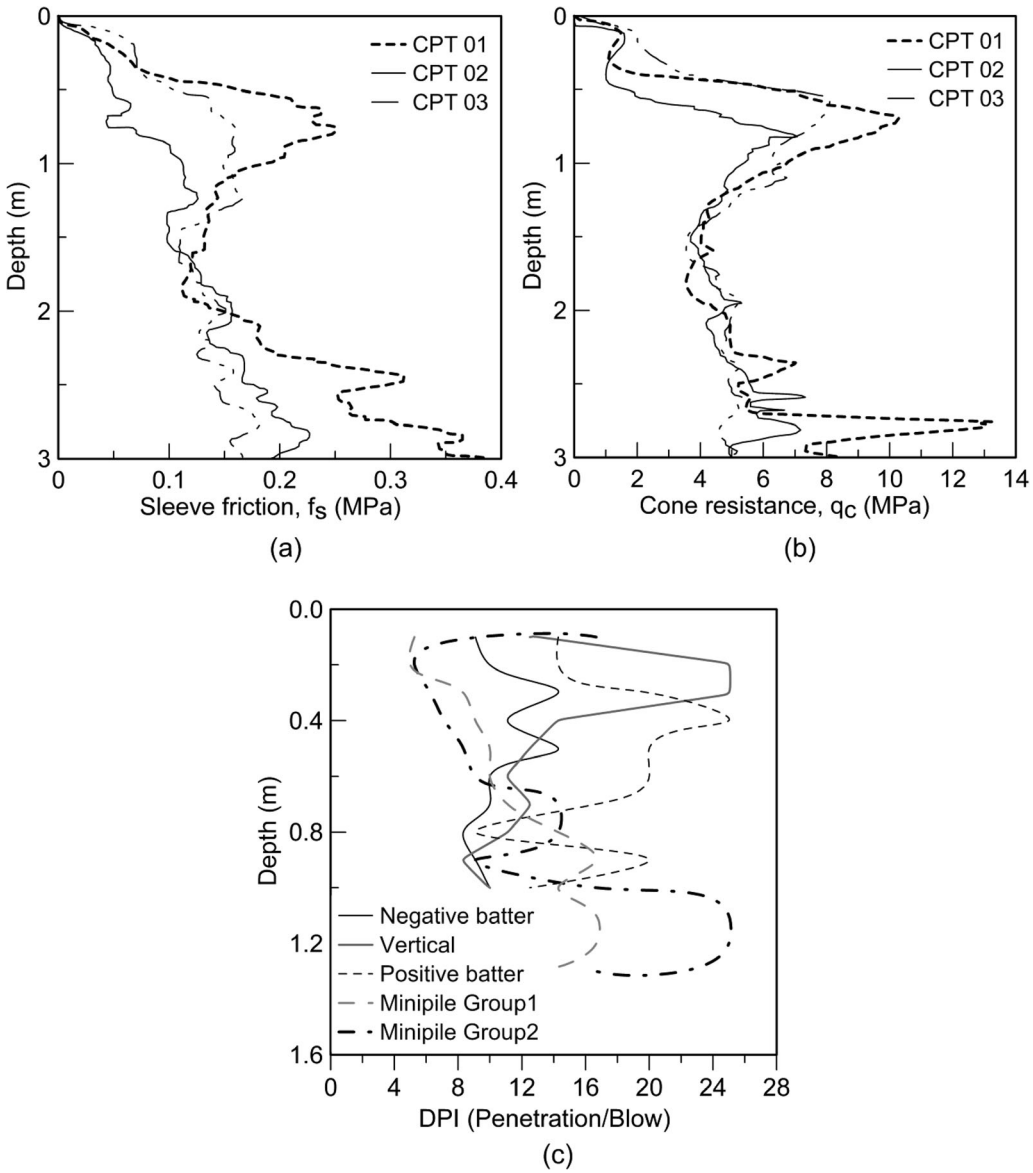


**Fig. 2** a Sleeve friction, **b** cone resistance around the test site, and **c** DCP results adjacent to the test location

bonded with two-part epoxy as shown in Fig. 3a, b. The minipiles were calibrated in the lab before testing in the field to account for any change in stiffness caused by the groove and the applied epoxy. For the calibration process, the minipile was fixed at one end and subjected to incremental loading at the other end, similar to a cantilever beam, as shown in Fig. 3c. Strain gauges were also glued to the cured epoxy just above the FBGs to record the strain at each loading stage. The shift in wavelength due to temperature change was not considered, as quick load tests (within a minimally varying temperature range during the short period of tests) were to be performed in the field. The shift of wavelength was recorded using an Optical Spectrum Analyser (OSA) and analysed using a Gaussian fitting algorithm in MATLAB. The correlation between the shift of wavelength and the strain for the three minipiles used in the field experimentation is shown in Fig. 4.

## 2.4 Field static lateral load tests on single minipiles

Six single free-headed lateral load tests were performed: two vertically installed ($\theta = 0°$), two positively battered ($\theta = +25°$) and two negatively battered minipiles ($\theta = -25°$). The positive and negative batter describe the direction of inclination with respect to the loading, where 'positive' indicates inclination in the direction of the loading and vice versa for 'negative'. The optimum batter angle for laterally loaded minipiles in cohesive soil was reported to range from $\pm 25°$ to $\pm 45°$ [42]; hence, the

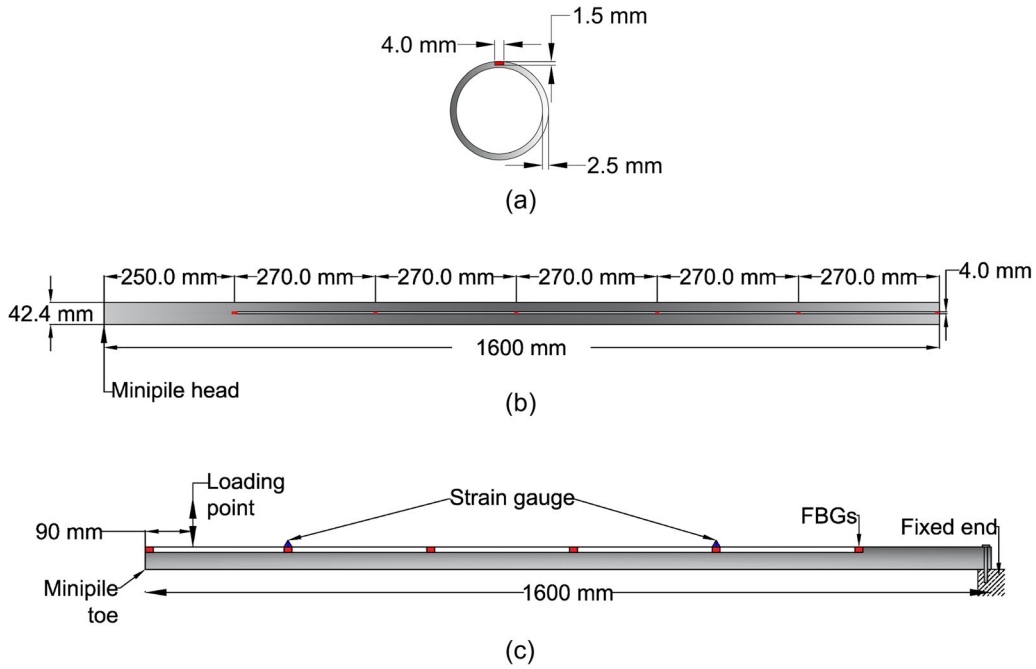


**Fig. 3** **a** Cross-sectional view of the minipile, **b** location of FBGs, and **c** calibration setup

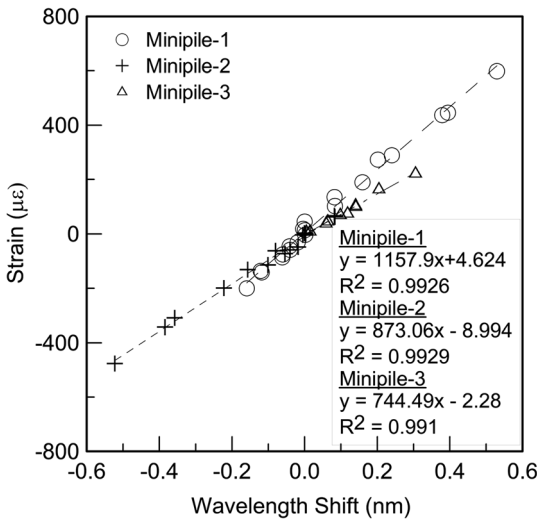


**Fig. 4** Correlation between the shift of wavelength and strain

lowest value of the range, 25°, was adopted in this study. Minipiles 1, 2 and 3 (Fig. 4) were used for vertical, positive, and negative conditions, respectively. The minipiles were driven into the ground with the aid of a handheld electric jackhammer. The net weight of the automated hammer was 18 kg, and the impact energy was 45 J with an impact rate of 1000 blows per minute. The minipiles were driven through the guiding sleeve, as shown in Fig. 5, to ensure a batter angle of 25° while driving and post-installation. Similar impact energy and the rate were imparted to all the minipiles during driving; however, the effect of installation was not the scope of this study, and it requires further investigation. Two minipiles (one instrumented and one with no instrumentation) were loaded simultaneously in the opposite direction and tested at a time, replicating a two-in-one setup [2, 53] (Fig. 5a). The distance between the minipile and the reaction minipile at ground level and toe level, for the + 25° condition, was 1.70 and 0.7 m, respectively, as shown in Fig. 5a. Similarly, the distance the θ = 0° and θ = − 25° conditions was 1.70 and 1.30 m, respectively. The vertical embedded depth of the minipiles at 0° was 1.27 m, and for the + 25° and − 25° conditions were 1.12 m. The load was applied at the ground level, and the vertical extension of the minipile above the mudline was maintained at 330 mm for all three battered angles to compare their behaviour under lateral load uniformly.

The quick lateral load test procedure was adopted from ASTM D3966/D3966M-07(2013) [7], and the lateral load was applied with a hydraulic jack and was recorded using a load cell and data logger (Fig. 5b). Each loading stage was maintained for 15 min so that the rate of the settlement was less than 0.25 mm/h following ASTM D1143 [6]. As the ultimate loads for different batter angles were not known, a consistent lateral load was applied in an incremental range of 1–2 kN until it became difficult to maintain the load applied by the hydraulic jack, and it required continuous jacking. The lateral head displacement was measured by two linear displacement transducers (LDT), and the optic fibre data was recorded using an interrogator.

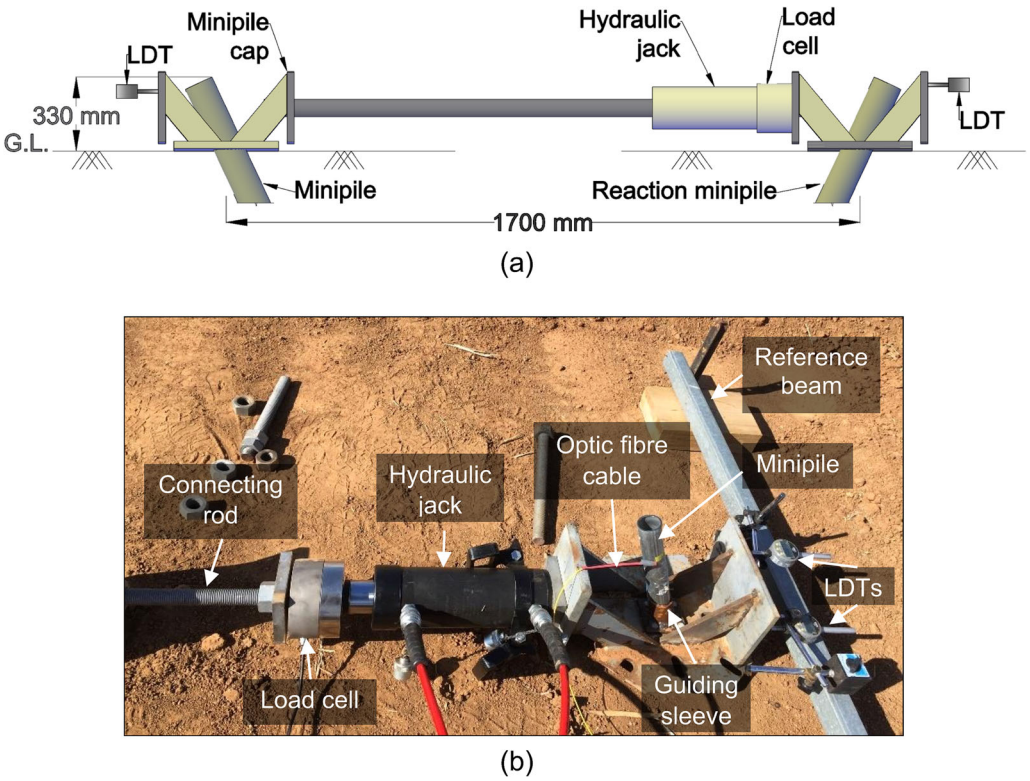


**Fig. 5** **a** Schematic of field test set-up for single minipiles and **b** general field-testing components

## 2.5 Field static lateral load tests on minipile groups

To investigate the interaction of minipiles when loaded in groups with different orientations, the lateral capacity of two types of minipile groups was also tested along with the single minipiles in the field at the same site, as mentioned earlier. The first minipile group, Mg1, had one positive (Mg1-3 in Fig. 6a), one negative (Mg1-1 in Fig. 6a) and two perpendicular outwardly (Mg1-2, Mg1-4 in Fig. 6a) battered minipiles. The second minipile group, Mg2, had two positively (Mg1-3, Mg1-4 in Fig. 6b) and two negatively (Mg1-1, Mg1-2 in Fig. 6b) battered minipiles. The orientation of the constituent minipiles in both types of groups, respectively, is shown in Fig. 6.

The design of Mg1 is broadly developed from the root architectures. Plate morphology is one of the prime categories of root system morphology where the basal roots either radiate laterally or obliquely from the thick main stem and offer three aspects of anchorage. In an oblique (heart) root system, the roots descend diagonally from the base. Mg1 is a simplified version of this root system with an R-type architecture which has inclined roots and the highest shear resistance among other root types [18]. Mg1 can also be observed as a blend of Marianna and Myrobalan root systems described in Burrall et al., [12]. The Myrobalan root system has steep main roots oriented laterally with branches near the base of the system, and the Marianna is an overall shallow root system. Similarly, Mg1 is a shallow-depth minipile group with steep laterally spreading branches (battered minipiles) close to the base of the system, the pile cap. Mg1 does not have the main branch, which is the central pile, to adapt to the reticulated root piles (RRP) design proposed by Lizzi [31]. Although the RRP is symmetric, Mg1 has an asymmetric design to minimise failure by rotation of the pile group when subjected to lateral loading. Hence, to engage a large volume of soil in resisting lateral or axial load similar to that of a tree root network in nature, this bio-inspired reticulated arrangement of minipiles (Mg1) was adopted.

Similar to the test configurations of single minipiles, grouped minipiles were also tested, replicating a two-in-one set-up (Fig. 7). Mg1 was loaded against Mg1 as shown in Fig. 7a, and similarly, Mg2 was loaded against Mg2 as shown in Fig. 7b to perform quick lateral load tests. The dimensions of the constituent minipiles were exactly similar to the single minipiles described earlier; however, for group tests, the minipiles were un-instrumented. The minipiles were battered at an angle of 25° and spaced at a distance ($S$) of almost $6B$ (254 mm) at the location of the pile cap. There was no relative rotation allowed between the pile head and the cap; hence, they can be categorised as fixed-headed battered minipile groups. The testing arrangement was the same as explained for the single

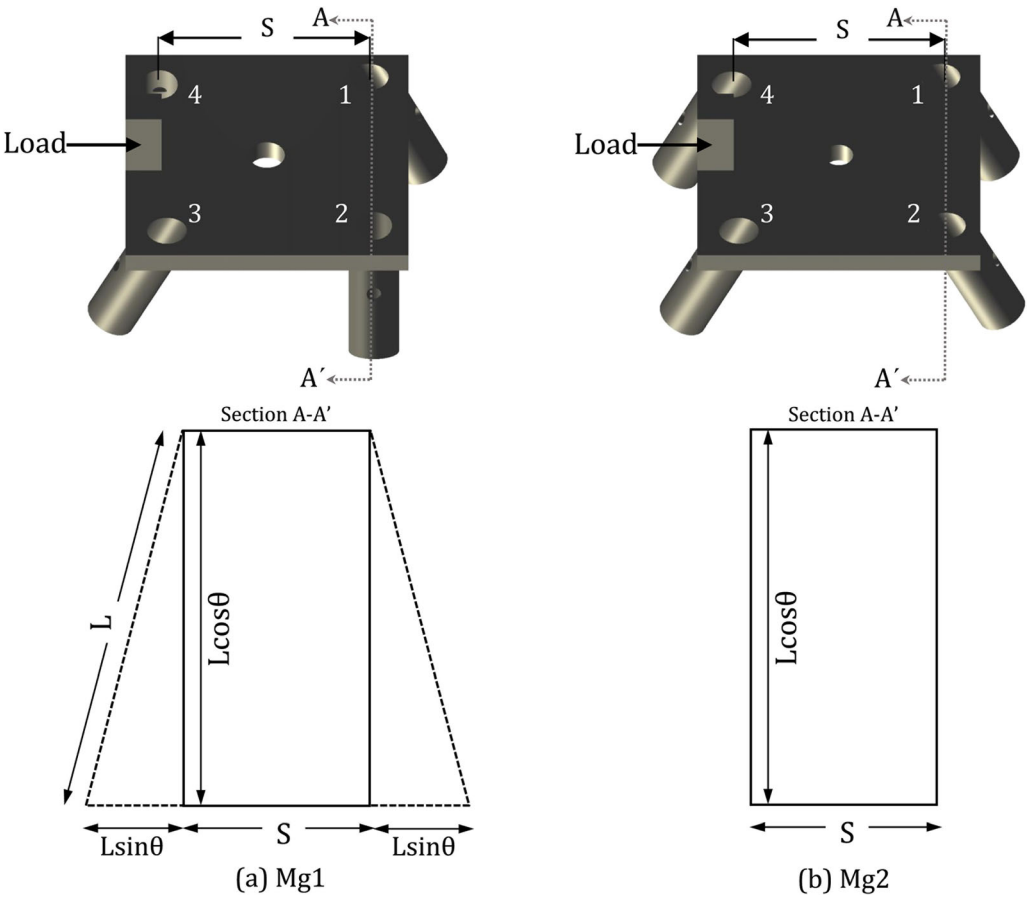


**Fig. 6** Schematic of minipile orientations and the projections of their bearing area for **a** Mg1 and **b** Mg2

minipiles, and two pile groups were loaded simultaneously against each other. First, Mg1 was tested for lateral resistance with small step intervals and based on the ultimate load achieved, the steps for loading Mg2 were set.

## 3 Results

### 3.1 Lateral load–displacement response of single full-scale minipiles

The data from the load cell and LDTs were used to produce the load–displacement plot at the minipile head. The lateral load tests were repeated twice using a two-in-one set-up, as mentioned previously, to confirm reproducibility and the load–displacement curves were found to be consistent. For clarity, data for the instrumented minipiles only are presented in Fig. 8. There are several criteria proposed to define the ultimate lateral load of a pile corresponding to a specified lateral head displacement or rotation [14]. Some of the proposed displacements based on the literature are 6 mm [35], 12.5 mm [59], 5% of the pile diameter ($B$) [8] or 20% of $B$ [9]. Since the minipiles are characteristically similar to a typical hollow pile but with a comparatively smaller diameter and shaft length, the criterion proposed by Broms [9] was adopted in this study. Accordingly, the lateral loads of the positively, vertically, and negatively battered minipiles at 8 mm lateral head displacement (20% of minipile diameter) were found to be 7, 4.2, and 3.2 kN, respectively. The highest lateral load capacity was observed for the + 25° configuration, followed by the 0° and − 25° battered minipiles, in accordance with the widely reported findings in the literature [28, 50, 62]. As the values of undrained shear varied within a very small range of 36–40 kPa for the corresponding locations of single minipiles, the effect of stratigraphy on load-bearing capacity can be eliminated. It can also be deciphered that the divergence between the vertical and negative cases is not as high as that between positive and the other two cases, as shown in Fig. 8. It is observed from the performance of negatively battered and vertically installed minipiles that on average, the lateral resistance of 0° is 25.6% higher than − 25° minipile in medium stiff clay.

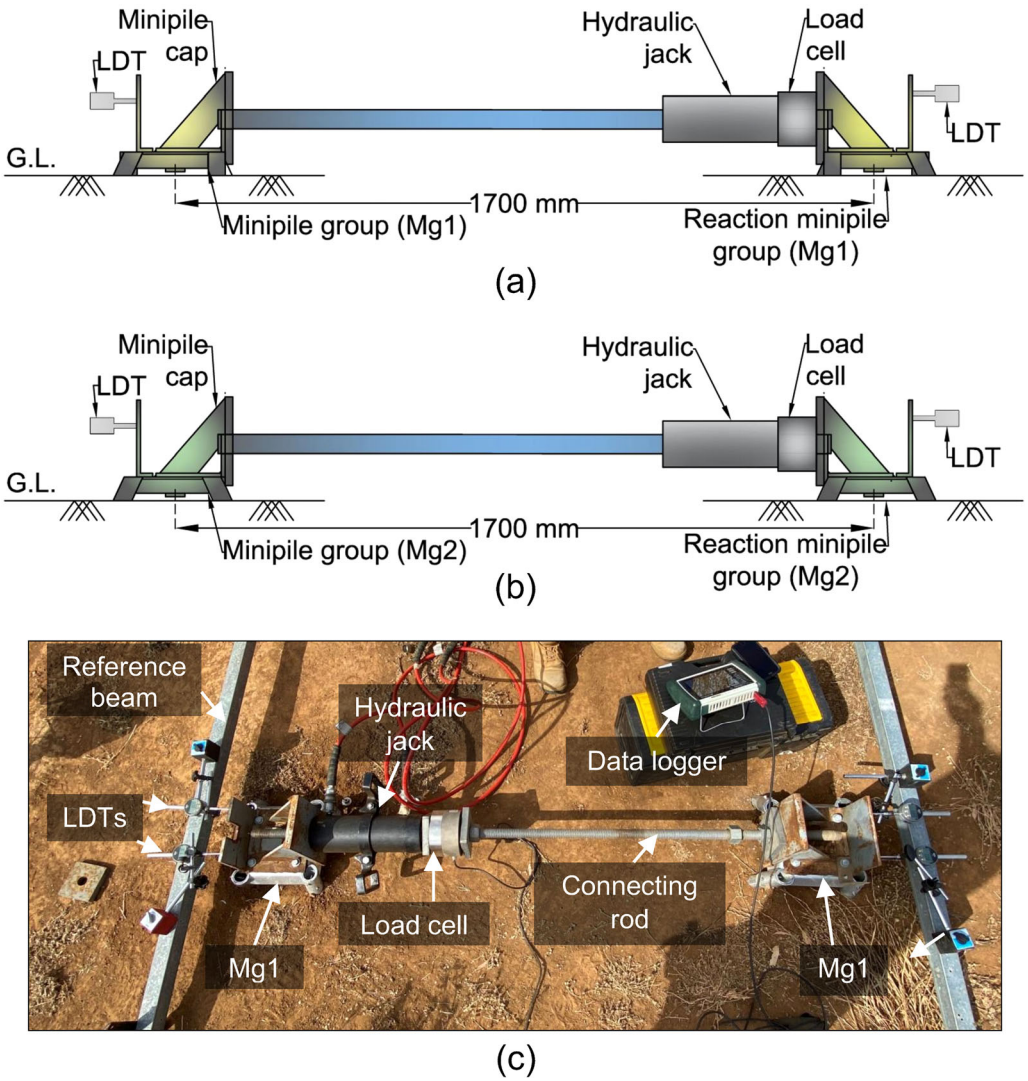


**Fig. 7** Schematic of field test set-up for minipile group **a** Mg1, **b** Mg2, and **c** general field-testing components

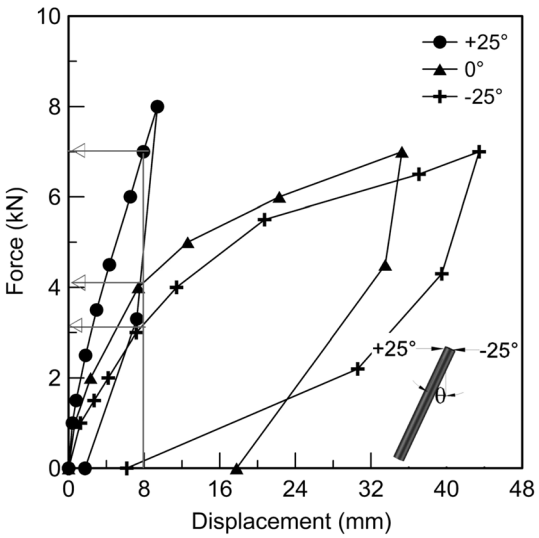


**Fig. 8** Force–displacement curves of single minipiles

### 3.2 Strain profile

The optic fibre data was analysed to produce the strain profile along the minipile shaft, as shown in Fig. 9, corresponding to each loading stage (− 0.0 kN indicates after complete unloading) for 0° (Fig. 9a), + 25° (Fig. 9b) and − 25° (Fig. 9c) battered minipiles. As the optic fibres are installed on the face that is pushed against the soil, the positive recorded strain is compressive, which is observed to increase with increasing load. The tensile strain was not recorded and reported in this study as the objective of the optic fibre was to obtain a strain profile to validate the numerical model, and one set of data was found to be adequate. The maximum strain is observed at a depth of 0.8 m for the battered cases and slightly higher for the vertical case. At any particular load, the pile head displacement is lowest for the positive case; hence, the strain

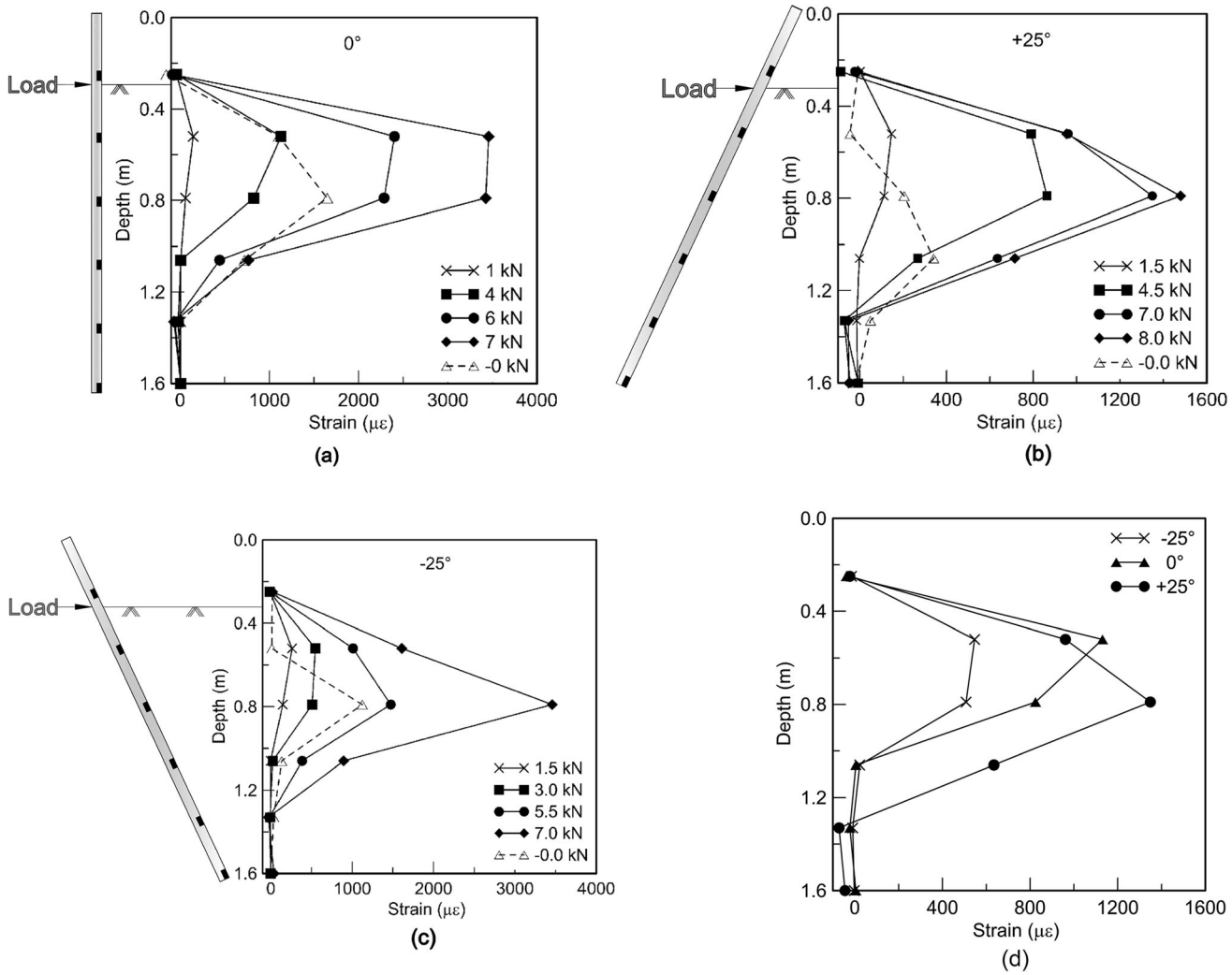


**Fig. 9** Strain profiles along the full-scale minipile **a** vertical, **b** positive, **c** negative battered, and **d** strain profile at 8 mm lateral head displacement

recorded is also the least. The force–displacement curves for the 0° and − 25° cases were nearly similar, and therefore, the maximum strain recorded at 7 kN loading is also similar in magnitude for both of them. It should be noted that the strain reported for the vertical minipile is due to bending only. However, for the battered cases, it is a combination of longitudinal and bending strain due to axial and lateral loads acting on the battered minipiles [51].

To compare the strain for all the three battered conditions, θ = 0°, θ = + 25° and θ = − 25°, the strain profile at the ultimate load is reviewed, which was considered corresponding to 8 mm lateral head displacement. The corresponding loads are 7, 4.2, and 3.2 kN for 0°, + 25°, and − 25°, respectively, from Fig. 8. The strain profile at 7 kN for θ = + 25°, 4 kN for θ = 0° and 3 kN for θ = − 25° are plotted in Fig. 9d, which shows maximum strain for + 25° followed by 0° and − 25°, respectively. This is attributed to the fact that at 8 mm lateral head displacement, the force sustained by + 25° is the highest, which in turn indicates that the passive soil pressure in front of the positive battered minipile is also the highest.

### 3.3 Lateral load–displacement response of full-scale minipile groups

The load–displacement curves of field testing on Mg1 and Mg2 are shown in Fig. 10. It can be seen that Mg1 shows a very stiff response compared to Mg2. Although both pile groups can be categorised as fixed-headed with a spacing of 6*B* at the pile head, the same embedment lengths and installation angles but different minipile configurations, they show very different lateral capacities. After 120 kN lateral loading on Mg1, the increase in displacement is substantial, and then the curve starts to get flatter, indicating plastic deformation dominating the soil response. For Mg2, however, a force of more than 27 kN could not

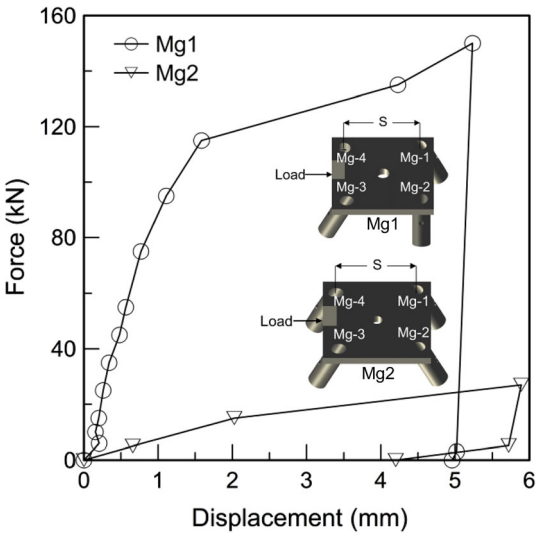


**Fig. 10** Force–displacement curves of minipile groups

be sustained, indicating an occurrence of ultimate load at 5.9 mm lateral head displacement. When the lateral load is applied to the minipile groups, the leading row is in compression, and the trailing row is in tension due to frame action. In the absence of vertical loading on the pile cap, the tension failure of the trailing minipiles controls the lateral load capacity of the minipile group [61]. This can be attributed to the observation of Mg2's lateral resistance getting mobilised at a very small displacement. For Mg1, the two perpendicularly battered minipiles resist rotation at the minipile head, hence, significantly increasing the lateral resistance. The bearing area, which is the projected area of the foundation on the plane perpendicular to the direction of loading, is said to be one of the key contributing factors in increasing the capacity of root systems [12]. The projected areas are demonstrated in Fig. 6a and b, respectively, where $S$ is the minipile spacing at the head, $L$ is the length of the minipile, $\theta$ is the batter angle, and $Lcos\theta$ and $Lsin\theta$ are the vertical and horizontal projections of the minipile length, respectively. The bearing area can be estimated as follows:

$$A_{Mg1} = (S + Lsin\theta) \times Lcos\theta \quad (4)$$

$$A_{Mg2} = S \times Lcos\theta \quad (5)$$

The bearing area of Mg1 is 3.06 times higher than that of Mg2; however, for battered pile groups subjected to lateral loading, only two-dimensional projection is not an adequate measurement of the volume of soil engaged in creating anchorage. Following the concept of bearing area, the projected area of a minipile group with four vertically installed minipile would be the same as that of Mg2, as shown in Fig. 6b. Since the lateral capacity of an individual vertically installed minipile is 4.2 kN (as mentioned in Sect. 3.1), considering a group efficiency of 100% at $6B$ pile-head spacing, the group capacity of $2 \times 2$ vertically installed minipile group would be 16.8 kN which is 61% lower than the reported capacity of Mg2 even though they have same bearing area. Thus, despite the similar projected area, the positive and negative orientation of the battered minipiles in Mg2 increases its lateral resistance furthermore. Likewise, the two-outward perpendicular minipiles in Mg1, Mg1-2 and Mg1-4 increase the zone of influence within the surrounding soil, and Mg1-1 and Mg1-3 add to the lateral resistance of Mg1 further due to their batter in the direction of loading. Irrespective of the direction from which lateral loading is applied, the response of Mg1 will be similar due to its asymmetric nature on all four sides of the minipile cap. However, Mg2 will respond differently when the lateral load is applied from any two adjacent faces of the minipile cap. This gives an added advantage to Mg1 when the direction of loading changes, especially in offshore conditions; however, it should be noted that diagonal loading was not considered in this study.

## 4 Numerical modelling

To investigate the behaviour of soil below mudline and obtain soil pressure, bending moment and axial force in a pile, numerical models on battered micropiles have been reported previously [21, 28, 41]. The pile-soil interaction can be evaluated meticulously using bending moment, axial force and horizontal soil-pressure distribution; however, these values cannot be straightforwardly measured by experimentation, especially below mudline. Hence, the group field tests were numerically simulated to understand the force–displacement curves obtained experimentally as the group minipiles were un-instrumented. In order to find the optimum pile head spacing for the battered minipile groups, parametric studies at three different minipile head spacings were also performed.

### 4.1 Description of finite difference model

The numerical simulation was performed using FLAC$^{3D}$, a finite difference software based on Lagrangian calculation, generally efficient for large deformation problems. The software's inbuilt structural element was used to generate the minipiles, while the soil block was modelled with zone elements. The soil zone was created using a hexahedral brick-shaped mesh with eight vertices. The edge length of the size of the mesh was optimised with respect to computational efficiency and structural response of the pile after simulating a wide range of mesh sizes. The width of the soil zone was 100 times the minipile diameter, and the depth was two times the minipile length below the minipile

toe to avoid boundary effects. These values were adopted by optimising computational cost and ensuring that there was no stress at the boundary of the model. The bottom face of the soil mesh was fixed, and the top surface of the soil was free in all three directions. Roller boundaries were applied to the side walls of the model, and they were fixed in the *x*-direction only. The geometric, material and interface properties were used to define the behaviour of a pile element with the surrounding soil.

An elasto-plastic Mohr–Coulomb constitutive model was used for the clay as this constitutive model has been previously used for simulating accurate behaviour of piles in clay by Mroueh and Shahrour [44] and Hazzar et al. [23], among others. It also requires only basic input parameters, which could be obtained from the in-situ site characterisation. Since only the ultimate failure criterion was given importance in this study over serviceability, the Mohr–Coulomb model was preferred over other advanced constitutive models, which increases computational cost and additional memory [19]. The pile-soil behaviour at the interface is controlled by normal and shear coupling springs that are both cohesive and frictional in nature. A linear Coulomb shear-strength criterion limits the shear force, normal and shear stiffness, dilation, tensile and shear bond strength that increases the effective normal force on the target face beyond the shear-strength limit. The inelastic constitutive model at the interface allows slip during large deformation, the absence of which has prevented accurate modelling of micropiles with higher ($> 45°$) batter angles [28]. The coupling spring parameters in shear are cohesive strength per unit length, $c_s$, stiffness per unit length, $k_s$ and friction, $\varphi_s$, which define the cohesion and friction interface properties. Similarly, the normal behaviour of the pile-grid interface is modelled by coupling cohesive strength per unit length, $c_n$, coupling stiffness per unit length, $k_n$, and coupling friction, $\varphi_n$. To calibrate the numerical tool, the soil properties were determined, and the model was tested for a range of $k_n$, $k_s$, $c_s$ and $c_n$ values that are reported in the following section.

### 4.2 Numerical analysis

The numerical model was validated with full-scale field investigation data on both individual minipiles and battered minipile groups (Fig. 11). For the Mohr–Coulomb constitutive model, the parameters obtained from the site characterisation—undrained cohesion of 38 kPa, Young's modulus of 14 MPa and unit weight of 19 kN/m$^3$ were adopted. These values were derived from the site characterisation data as mentioned earlier in the *Subsurface soil properties* section. Since the minipiles were subjected to quick lateral loading in the field, hence, an undrained loading condition was adopted, and total stress analysis was performed with zero excess pore water pressure. Thus, the angle of internal friction and dilation angle were assumed to be zero assuming completely saturated soil conditions. The $\phi = 0°$ analysis has been used for the calculation of bearing capacity and active and passive pressure in clay (A.W. Skempton) and gives conservative results. The values of cohesion, Young's modulus and unit weight of the soil were averaged over the embedment length of the minipile owing to the small length of the minipiles and also, the confining stress was expected to be low at such shallow depth. An isotropic condition was assumed for the initial in-situ stress conditions of the soil, and a gravitational equilibrium was first achieved. The structural pile element was then introduced into the model, and although the field installation was performed by driving the piles into the soil, the installation effects were neglected in the numerical model. It was assumed that the soil zone affected due to the application of lateral load would be larger than the area affected by the pile installation [4, 22]. This simplification was compensated by calibrating the stiffness properties at the interface of the piles with force–displacement curves obtained from full-scale testing, as explained further.

The properties of the minipile used in the numerical analysis are summarised in Table 1. The stiffness properties were calibrated for the battered minipiles using the experimental load–displacement curves (Figs. 8, 10). The $c_n$ was kept fixed at $1 \times 10^8$ N/m$^2$ for the constituent minipiles, and $c_s$ was equivalent to the undrained cohesion at the respective test location. Also, both $k_n$ and $k_s$ were of the order of $10^6$–$10^7$ N/m$^2$ for battered minipiles and $10^{13}$ N/m$^2$ for the perpendicularly outward battered minipiles, respectively.

The initial values were estimated using the relations [48],

$$k_n \approx 10\,(E_p/G)^{-0.14} \cdot G \tag{6}$$

$$\text{and } k_s \approx 1.6 \cdot G \tag{7}$$

where $E_p$ is Young's modulus of the pile, and $G$ is the shear modulus of the soil (obtained from CPT results). The $k_n$ was estimated to be $1.2 \times 10^7$ N/m$^2$, and $k_s$ was estimated to be $8.4 \times 10^6$ N/m$^2$. However, these relations were proposed for vertically installed piles and hence, they required further adjustments for modelling battered piles with unique orientations. Although the order of $k_n$ and $k_s$ was appropriate for the positive and negative battered minipiles; however, for the perpendicularly outward battered minipiles, a higher value of $k_n$ and $k_s$ was required to calibrate the numerical model with the field results, which was of the order $10^{13}$. The calibrated stiffness properties for minipile groups are summarised in Table 2.

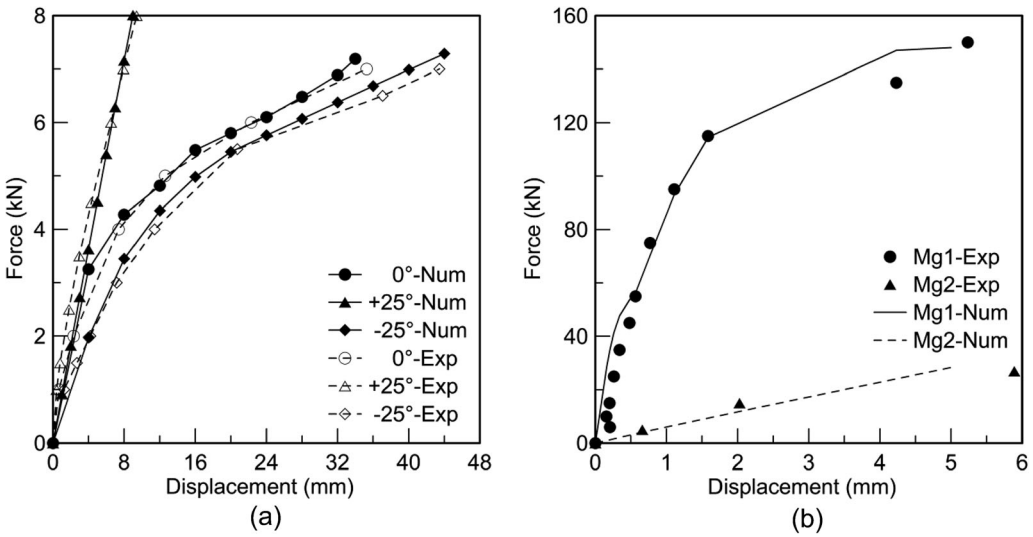


**Fig. 11** Comparison of force–displacement curves obtained from experiment and numerical model for **a** single minipiles and **b** minipile groups

**Table 1** Mechanical properties of the full-scale minipiles

| $E_p$ (N/m$^2$) | Area (m$^2$) | Perimeter (m) | $I_y$[a] (m$^4$) | $I_z$[b] (m$^4$) | J[c] (m$^4$) | $\mu$[d] |
|---|---|---|---|---|---|---|
| $2 \times 10^{11}$ | $3.13 \times 10^{-4}$ | 0.133 | $1.25 \times 10^{-7}$ | $1.25 \times 10^{-7}$ | $2.5 \times 10^{-7}$ | 0.30 |

[a]Second moment with respect to y axis, [b]second moment with respect to z axis, [c]Polar moment of inertia, and [d]Poisson's ratio

**Table 2** Coupling spring parameters in numerical model

| Minipiles | $k_n$[a] (N/m$^2$) | $k_s$[b] (N/m$^2$) | $c_n$[c] (N/m$^2$) | $c_s$[d] (N/m$^2$) |
|---|---|---|---|---|
| Mg1-1, Mg1-3 | $4 \times 10^{13}$ | $4 \times 10^{13}$ | $1 \times 10^{8}$ | $52 \times 10^{3}$ |
| Mg1-2, Mg1-4 | $1.2 \times 10^{7}$ | $8.4 \times 10^{6}$ | $1 \times 10^{8}$ | $52 \times 10^{3}$ |
| Mg2-1, Mg2-2, Mg2-3, Mg2-4 | $1 \times 10^{6}$ | $1 \times 10^{6}$ | $1 \times 10^{8}$ | $45 \times 10^{3}$ |

[a]Normal coupling stiffness, [b]shear coupling stiffness, [c]normal coupling cohesion, and [d]shear coupling cohesion

### 4.3 Numerical simulation of full-scale minipiles

The validated force–displacement plot of the individual full-scale minipiles is shown in Fig. 11a, where 'Num' denotes numerically obtained plots and 'Exp' denotes force–displacement curves from full-scale field investigation of single minipiles. A tension gap was observed on the active side of the minipiles in the field, which was simulated and observed in the numerical model as well. It was noted from the numerical simulation that the passive pressure in front of the negative battered minipile was lower than that for the positively battered minipile. This reduction in soil pressure for the battered case where the load is applied in the direction opposite to the batter was also reported by Rao and Veeresh [50] using *p-y* curves derived from the strain profile. The observed reduction in passive pressure between + 25° and − 25° is almost 2.35 times and should be taken into account when predicting the lateral load capacity of negative battered minipiles in practice.

Lateral load tests on full-scale minipile groups were simulated using their respective calibrated numerical models to obtain bending moments, horizontal stresses and axial force distributions. The two full-scale minipile groups presented previously were modelled numerically using the stiffness parameters mentioned above. However, the apparent cohesion of the soil was adjusted based on different in-situ test data obtained from site characterisation adjacent to the location of these tests, as explained earlier. The validated force–displacement plot of the full-scale minipile groups simulated until 5 mm lateral head displacement is shown in Fig. 11b.

#### 4.3.1 Bending moment, axial force and horizontal stress contour

The bending moment profiles of the constituent battered minipiles of the groups were acquired to compare the minipile group's behaviour in clay. Figure 12a shows the bending moment at 5 mm head displacement (since Mg1 was terminated at 5 mm) of the minipile cap. As observed in Fig. 12a, Mg1 sustains a much higher bending moment compared to Mg2, as at the same lateral head displacement, the force resisted by Mg1 was also much higher. The location of occurrence of the maximum bending moment depends on the rotation of the pile head [63]. In this study, the minipile group cap is allowed to rotate; however, the relative rotation between the cap and the minipile head is restrained. Hence, the maximum moment occurs near the cap, which is in agreement with the findings of McVay et al., [37] for fixed-head battered pile groups. Figure 12a also suggests that for both Mg1 and Mg2, respectively, the bending moments of the trailing and leading minipiles are the same. When it comes to the effect of the orientation of minipiles, for Mg1, the bending moments in Mg1-2 and Mg1-4 (minipiles perpendicular to the axis of loading; Fig. 6) close to the minipile cap were significantly lower than in Mg1-1 and Mg1-3 (minipiles in the axis of loading; Fig. 6). This indicates that Mg1-2 and Mg1-4 resisted the rotation of the minipile cap.

In battered minipiles, part of the lateral load is sustained by axial resistance. Thus, to further understand the axial force distribution in the constituent minipiles, the axial

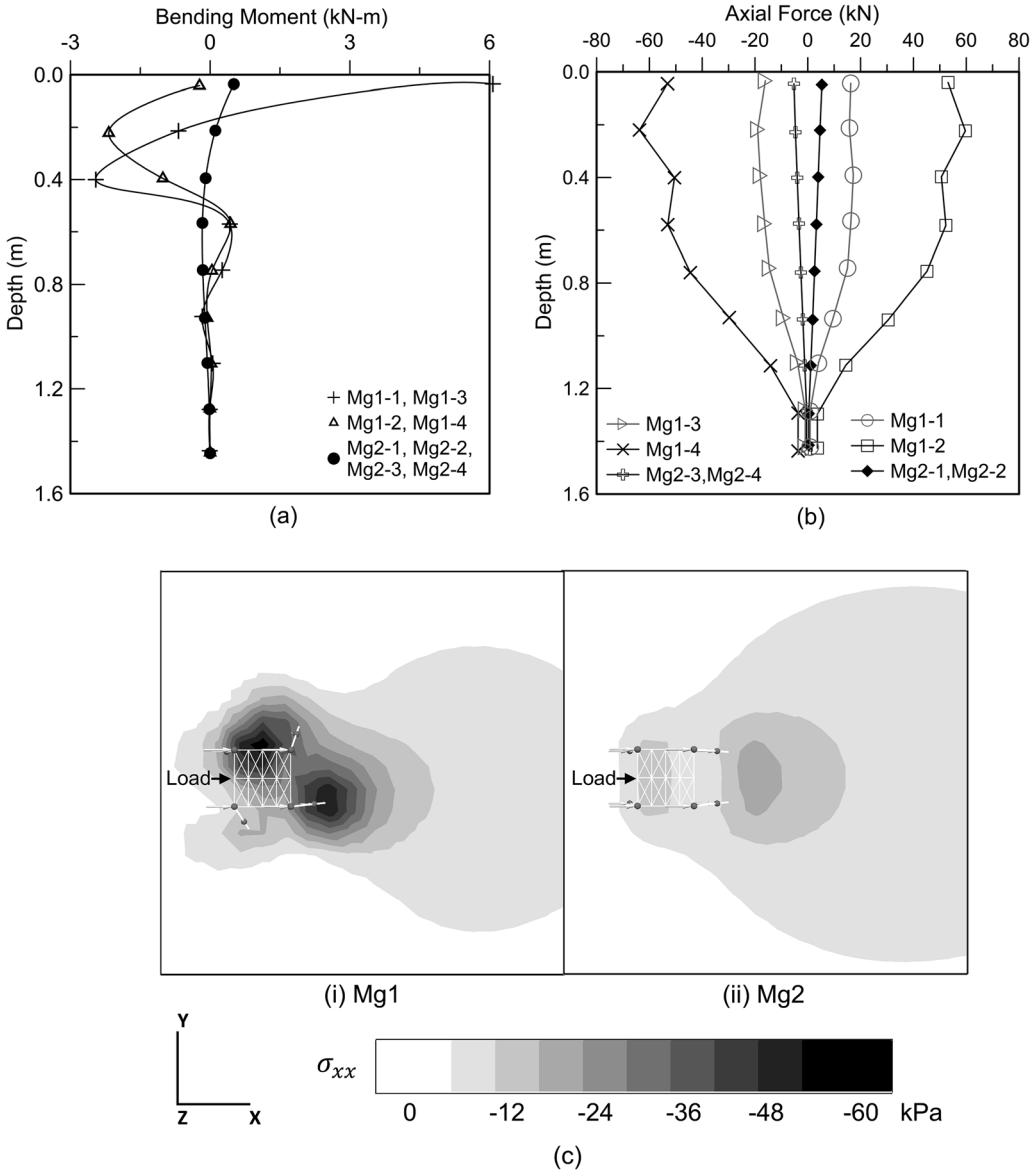


**Fig. 12** **a** Bending moment, **b** axial force and **c** horizontal soil pressure (at 8 mm displacement) for minipile groups from numerical analysis

force distribution was obtained from the numerical model and plotted with vertical depth for tested minipile groups. Figure 12b depicts that the axial resistance of Mg1 is much higher compared to that of Mg2. Looking further into the impact of minipile orientation, Mg1-2 and Mg1-4 (minipiles perpendicular to the axis of loading) carry a substantial proportion of lateral load in the form of the axial component. The leading and trailing minipiles are in compression and tension, respectively, with each row carrying an equal magnitude of axial load, similar to what is reported in Fig. 12a with bending moments.

The horizontal soil pressure ($\sigma_{xx}$) distribution was recorded from the numerical model to visualise whether there was an overlapping of shear zones. Figure 12c shows the stress on the XY-plane at a depth of 5*B* from the ground level at 5 mm head displacement of the minipile caps. As evident from Fig. 12c, the magnitude of the horizontal soil stress in the vicinity of Mg1 is almost three times higher than for Mg2. For Mg2, stress bulbs of the leading and trailing minipiles do not interact much with each other; however, the minipiles on the same side have overlapping stress zones. For Mg1, nevertheless, all four minipiles have independent stress bulbs, and in addition, the perpendicular minipiles increase the influence area, engaging a larger soil volume. These are some of the reasons why Mg1 exhibited a higher load-carrying capacity than Mg2. Thus, in fine-grained soil, the resistance of Mg1 to transverse loading is higher mainly due to the contribution of two perpendicular battered minipiles, which increases the tensile resistance of the trailing row, prevents the rotation of the minipile cap and also increases the volume of soil engaged. This outcome corroborates the fact that when the central column of a tree root extends radially rather than continuing vertically, it increases the load-bearing capacity, as reported by Burrall et al., [12].

#### 4.3.2 Effect of pile spacing

The numerical model was further adopted to investigate the effect of pile spacing on the behaviour of minipile groups advancing the overall concept of root geometry and spacing. Three different spacings of three (3*B*), five (5*B*) and six (6*B*) times the minipile diameter for the minipile groups, Mg1 and Mg2, were adopted. The force–displacement curve indicated that as the pile spacing increased from 3 to 6*B*, the lateral resistance of the minipile groups (both Mg1 and Mg2) increased, consistent with the literature [13, 36]. The pile deflection patterns for Mg1 and Mg2 at 5 mm lateral head displacement, as obtained from the numerical model, are shown in Fig. 13a and b, respectively (in the legend, Mg1-1-3*B* indicates minipile Mg1-1 at 3*B* spacing and, so on). At 5 mm lateral head displacement, the overall deflection of Mg1 is lower than Mg2, which is representative of the latter's lower lateral resistance, as also obtained from the field experimentation. Due to the difference in orientation of battered minipiles in Mg1 and Mg2, their deflection patterns are also different from one another. Also, at each spacing, there was almost no difference in deflection pattern between the leading and trailing minipiles, even at a lower spacing of 3*B*. This is consistent for both types of minipile groups studied here. Nevertheless, for Mg1, the deflected shapes of Mg1-1 and Mg1-3 are different from Mg1-2 and Mg1-4 due to their orientation directions in the group. For Mg1, as the spacing was reduced from 6 to 3*B*, the deflection of the negative and positive battered minipiles, Mg1-1 and Mg1-3, increased due to pile-soil-pile interaction, as was also reported by Chandrasekaran et al., [13] for vertically installed minipile groups. The decrement in spacing, however, did not affect the deflection profile of perpendicularly battered minipiles, Mg1-2 and Mg1-4. For Mg2, the overall lateral deflection of minipiles in the group at 3*B* spacing was quantitatively lower than at 5*B* and 6*B*, respectively, which is in contrast with the observation of Mg1.

The bending moment profile as shown in Fig. 13c and d, indicates different patterns for both Mg1 and Mg2 similar to their deflected shapes. The bending moment recorded for Mg1 is almost ten times higher than Mg2 at 5 mm lateral head displacement; however, at the same lateral load, Mg1 sustains a much lower bending moment compared to Mg2. Since at the same load, the moment for Mg1 is lower than Mg2, Mg1 can be used as an alternative pile group to reduce bending at critical depths. The bending moment for Mg2 is higher at greater depth due to softening of soil caused by group interaction, as also reported by Chandrasekaran et al., [13]. The moment recorded by the leading and trailing minipiles for Mg1 and Mg2 configurations is nearly similar, as also reported by Abu-Farsakh et al. [3], except at 3*B* spacing. At a lower minipile spacing of 3*B*, for Mg1, the absolute value of bending moment recorded for Mg1-1 is almost three times the value observed for Mg1-3 at 1.068 m below mudline. Also, the bending moment at 1.068 m below mudline for Mg2-1 and Mg2-2 is double of Mg2-3 and Mg2-4. The higher bending moment in the leading row of minipiles is indicative of the shadowing effect at 3*B* spacing. This shadowing effect has been reported extensively for vertically installed pile groups by Brown et al. [10] and Rollins et al. [56], among others. However, there is no discrepancy in bending moments between trailing and leading rows of the outwardly battered minipiles (Mg1-2 and Mg1-4) in Mg1.

As the spacing in the battered minipile groups increases from 3 to 6*B*, the shadowing effect diminishes even in stiff clay, and the individual minipiles offer higher lateral resistance, similar to or even better than when installed in

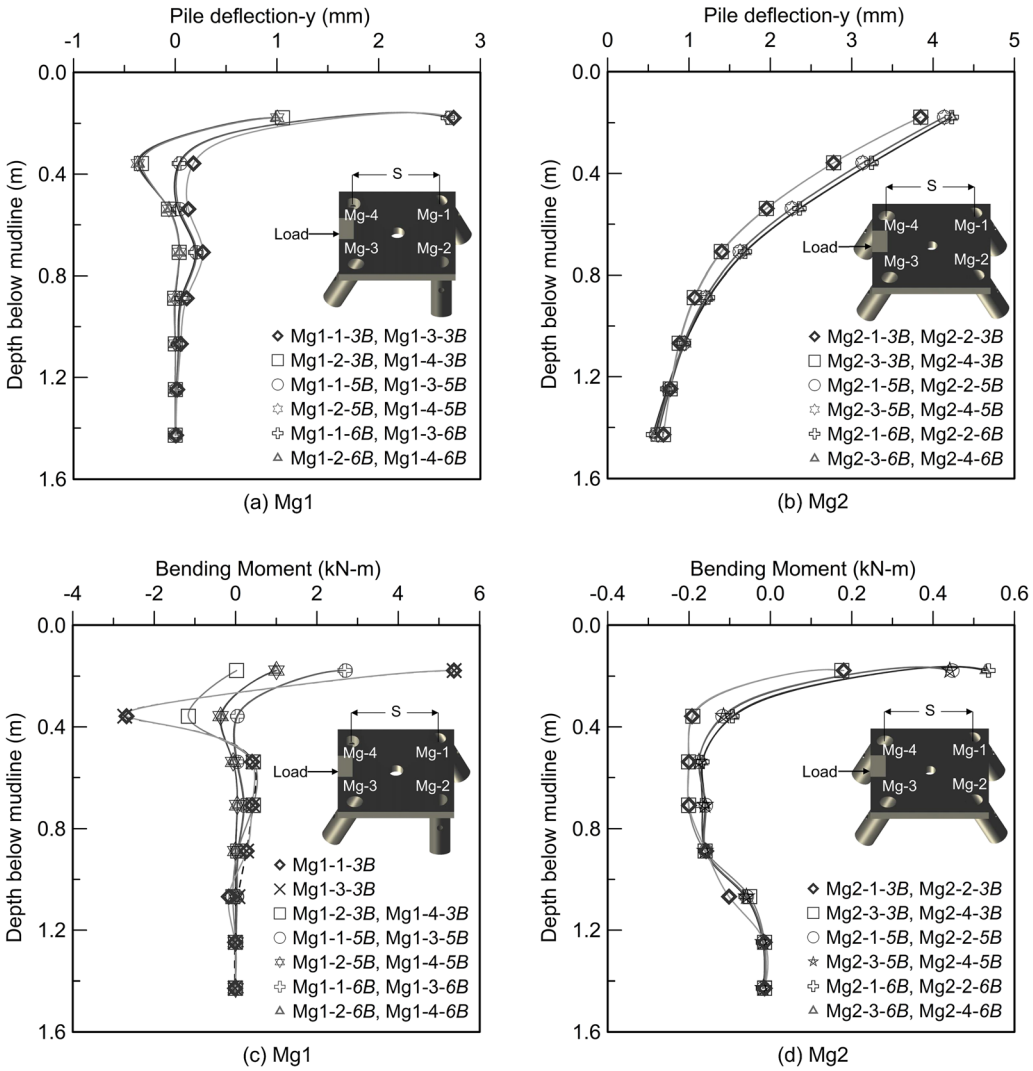


**Fig. 13** Deflection pattern for **a** Mg1 and **b** Mg2, and bending moment for **c** Mg1 and **d** Mg2 at 5 mm lateral head displacement from numerical analysis

isolation. Thus, among the limited pile group spacings investigated in this study, 6*B* can be proposed as the optimum pile head spacing. This results in group efficiency greater than 100% as also mentioned by Reese et al., [52]. Thus, *p*-multiplier values greater than unity can be expected from the minipile groups, Mg1 and Mg2, at 6*B* spacing in this study. The *p*-multipliers can be estimated from the *p*-*y* curves, which, in turn, can be back-calculated from the bending moment profiles, as shown in Fig. 13c and d. The *p*-*y* curves are the soil resistance versus lateral pile displacement at any depth of the minipile.

From the soil pressure distribution profile, the maximum soil resistance was found to occur at a depth of 0.18 m (4.2*B*) below the mudline for both Mg1 and Mg2. The *p*-*y* curves at 5 mm displacement were back-calculated from the bending moment curves using a similar technique described in Chandrasekaran et al., [13] and are shown in Fig. 14a and b for Mg1 and Mg2, respectively, at a depth of 4.2*B* below mudline. With the decrease in pile spacing from 6 to 3*B*, the soil reaction curves became softer, indicating a shadowing effect for minipile groups. For Mg1 in Fig. 14a, the soil reaction of Mg1-1 and Mg1-2 are minutely lower than Mg1-3 and Mg1-4, respectively, although the former is in the leading row. A similar pattern can also be seen for Mg2 in Fig. 14b at 3*B* spacing and this is due to the orientation of the battered minipiles in the group. It should be noted that the leading row has negatively battered minipiles, and similarly, the trailing row has positively battered minipiles, and the load-carrying capacity of a single positively battered minipile is much higher as found experimentally (Fig. 8).

The *p*-*y* curves are commonly used to calculate *p*-multipliers; however, given the difference in undrained shear strength at the test location of single and grouped battered

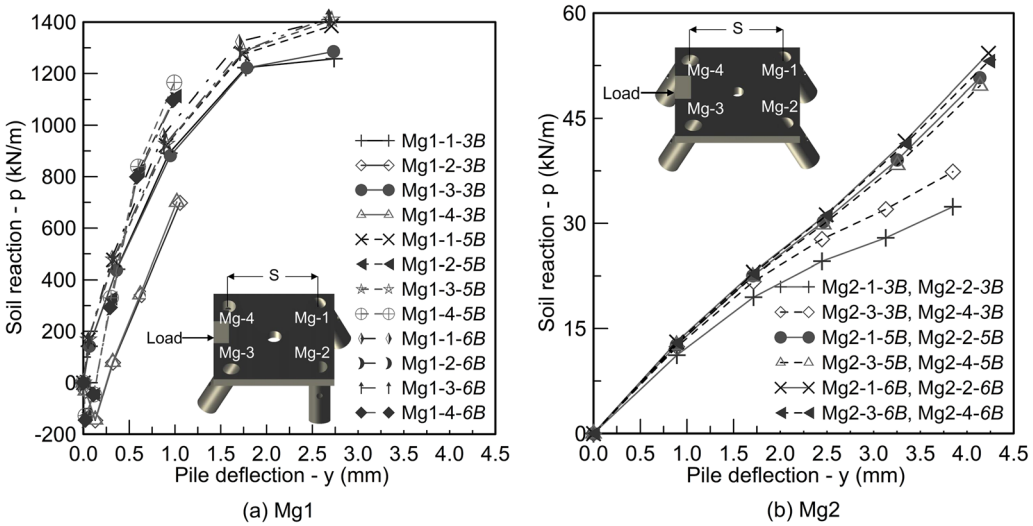


**Fig. 14** *p-y* Curves of the constituent minipiles at 4.2B depth below mudline for **a** Mg1 and **b** Mg2 from numerical analysis

minipiles; it is not accurate to use the single minipiles' results to estimate the *p*-multipliers. Nevertheless, concluding remarks about the non-occurrence of the shadowing effect at 5*B* and 6*B* spacing for battered minipile groups can be drawn from the *p-y* curves, indicating a value of *p*-multiplier of at least unity or even higher.

Although the numerical model was calibrated with field experiments, it has some limitations. The excess pore water pressure developed during the driving of the minipiles was not allowed to dissipate completely and return to the pre-installation hydrostatic condition of the field. The DCP tests were performed adjacent to the test locations, yet it does not capture the change in soil properties post-installation, and hence, the installation effect was not accurately depicted in the numerical model. Also, the soil plugging effect was neglected in this study owing to the small diameter of the minipile. Thus, a further advanced numerical model is essential and until then, this investigation can be used as a primary source of reference.

## 5 Discussion

Although bio-inspired tree root systems have been long discovered and applied in the form of underpinning that replicates the roots of a tree [31], their design has not been further improvised or evolved. The performance of pile foundations and soil anchorage systems have been identified as a potential area to be benefitted from the bio-inspired approach. In addition to the physical replication of tree root systems, their behaviour or principles can also be adopted depending on the type of engineering solution we wish to achieve. Previous studies report pullout tests performed on root structures in their original form; however, this research reports the translation of features such as angle and level of branching and relative stiffness of root into a prototype shallow foundation system. An approximate adaptation of the form of root architecture was only studied here as both the biological context and geotechnical application are almost similar. This study upscales the biological strategy and evaluates the performance at the system level, paving the way for further levels of abstraction. The limitations that were mentioned in the literature from the upscaling and the disparity between biological and engineering materials were also somewhat bridged.

However, there are additional aspects of tree root systems that have not been adopted in this study, such as the system mass and spatial non-linearity. Further studies are recommended to implement the tapering thickness of battered piles and other orientations of individual battered piles within a pile group. The biological features such as self-healing properties, adaptation to dynamic environmental conditions, shape-change feature, varying surface texture and composite material properties of the roots are yet to be explored. In terms of material, only steel pile was considered here, while a vast opportunity still remains in exploring other complex materials that could have varied surface roughness and self-healing properties and could also simulate both flexible and rigid behaviour of roots. In summary, the multifunctional attributes of a tree-root-inspired foundation and the interaction among the individual facets require further in-depth study. The bio-inspired landscape that is yet to be explored in terms of implementation is anticipated to improve sustainability and resilience in the built environment.

## 6 Conclusion

This study aimed to understand the load-transfer mechanism of a simplified nonlinear branched foundation design inspired by a tree root system. The scaling and technical feasibility of the root systems were taken into consideration to introduce an asymmetric branched foundation that possesses higher lateral load capacity than the conventional branched group. The conclusive remarks are as follows,

(i) The experimentally obtained load–displacement curves (Fig. 8) of the single minipiles indicate that the positive 25° carries the maximum lateral load, followed by the vertically installed minipile and negative 25° battered minipile having the least lateral resistance, respectively.

(ii) The asymmetric minipile group with two perpendicularly battered minipiles (Mg1) carried almost five times more lateral load than the conventional battered minipile group configuration (Mg2) due to the engagement of a larger volume of soil and increased bearing area for Mg1 as depicted in Fig. 10.

(iii) The numerical model results show that for the group with two perpendicularly battered minipiles (Mg1) in clay, the bending moment of the minipiles in the loading axis was significant near the pile cap. However, bending moments for the perpendicular minipiles were considerably lower in Mg1 (Fig. 12a).

(iv) The axial load carried by the perpendicular minipiles in Mg1 was substantial compared to the minipiles in the axis of loading, which increased the horizontal load capacity of Mg1 compared to Mg2 (Fig. 12b).

(v) The numerical model was further used to investigate the effect of pile head spacing on the minipile groups. The increment of pile head spacing from 3 to 6*B* had no significant effect on the deflection pattern of the constituent minipiles in the group (Fig. 13a, b). At 3*B* spacing, the bending moment of the leading minipiles was higher than that of trailing minipiles in both battered pile groups, indicating a shadowing effect in clay (Fig. 13c, d). Also, as the spacing was reduced from 6 to 3*B*, the soil reaction curves became softer due to the overlapping of shear zones.

(vi) Although Mg2 is the conventional battered pile configuration that is being used in practice, the new type of bio-inspired group configuration investigated in this study which represents a tree root network performed better in terms of lateral load resistance.

**Acknowledgements** The first author thanks The University of Melbourne for offering the Melbourne Research Scholarship.

**Author contributions** All authors contributed to the study, conception and design. Material preparation, data collection and analysis were performed by SM. The first draft of the manuscript was written by SM, and MD and AM commented on previous versions of the manuscript. All authors read and approved the final manuscript.

**Funding** Open Access funding enabled and organized by CAUL and its Member Institutions. This research was funded by the Australian Research Council Linkage scheme (project ID LP160100828). Besides, the authors acknowledge the financial and in-kind support provided by Surefoot Pandoe Pty Ltd.

**Availability of data and materials** All of the data and models that support the findings of this study are available from the corresponding author upon request.

**Code availability** The code used for numerical simulation is available from the corresponding author upon request.

## Declarations

**Conflict of interest** The authors have no conflicts of interest to declare that are relevant to the content of this article.

**Ethical approval** Not applicable.

**Consent to participate** Not applicable.

**Consent for publication** Not applicable.



## References

1. AASHTO LRFD bridge design specifications (2012) American association of state highway transportation officials, Washington, DC
2. Abd Elaziz AY, El Naggar MH (2015) Performance of hollow bar micropiles under monotonic and cyclic lateral loads. J Geotech Geoenviron Eng 141(5):04015010
3. Abu-Farsakh M, Souri A, Voyiadjis G, Rosti F (2018) Comparison of static lateral behavior of three pile group configurations using three-dimensional finite element modeling. Can Geotech J 55(1):107–118. https://doi.org/10.1139/cgj-2017-0077

4. Achmus M, Kuo Y-S, Abdel-Rahman K (2009) Behavior of monopile foundations under cyclic lateral load. Comput Geotech 36(5):725–735
5. AS 1289.6.3.2 (1997) Methods of testing soils for engineering purposes—method 6.3.2: soil strength and consolidation tests-determination of the penetration resistance of a soil-9kg dynamic cone penetrometer test, Australian Standard, Sydney, New South Wales, Australia
6. ASTM D1143 (2020) Standard test methods for deep foundation elements under static axial compressive load. ASTM International
7. ASTM D3966 (2013) Standard test methods for deep foundations under lateral load. ASTM International
8. Briaud J (1984) Panel discussion, laterally loaded deep foundation (STP 835). ASTM, Philadelphia, pp 239–243
9. Broms BB (1964) Lateral resistance of piles in cohesionless soils. J Soil Mech Found Div 90(3):123–158
10. Brown DA, Morrison C, Reese LC (1988) Lateral load behavior of pile group in sand. J Geotech Eng 114(11):1261–1276. https://doi.org/10.1061/(ASCE)0733-9410(1988)114:11(1261)
11. Brown DA, Reese LC (1988) Behavior of a large-scale pile group subjected to cyclic lateral loading, Texas University at Austin
12. Burrall M, Dejong JT, Martinez A, Wilson DW (2020) Vertical pullout tests of orchard trees for bio-inspired engineering of anchorage and foundation systems. Bioinspir Biomim 16(1):016009
13. Chandrasekaran S, Boominathan A, Dodagoudar G (2010) Group interaction effects on laterally loaded piles in clay. J Geotech Geoenviron Eng 136(4):573–582
14. Chen Y-J, Lee Y-H (2010) Evaluation of lateral interpretation criteria for drilled shaft capacity. J Geotech Geoenviron Eng 136(8):1124–1136. https://doi.org/10.1061/(ASCE)GT.1943-5606.0000325
15. Danistan J, Vipulanandan C (2009) Relationship between CBR values (un-soaked) and undrained shear strength of artificial CH soils. CIGMAT-2009 Conference
16. Doherty P, Igoe D, Murphy G, Gavin K, Preston J, Mcavoy C, Byrne BW, Mcadam R, Burd HJ, Houlsby GT, Martin CM, Zdravković L, Taborda DMG, Potts DM, Jardine RJ, Sideri M, Schroeder FC, Muir Wood A, Kallehave D, Skov Gretlund J (2015) Field validation of fibre Bragg grating sensors for measuring strain on driven steel piles. Géotech Lett 5(2):74–79. https://doi.org/10.1680/geolett.14.00120
17. Douglas JG, Ferguson J, Douglas JG (1988) Geology of Victoria. Geological Society of Australia Melbourne, Australia
18. Fan C-C, Chen Y-W (2010) The effect of root architecture on the shearing resistance of root-permeated soils. Ecol Eng 36(6):813–826
19. FLAC (2008) 3D manual: a computer program for fast Lagrangian analysis of continua (Version 4.0), Minneapolis, Minnesota, USA
20. Frost JD, Martinez A, Mallett SD, Roozbahani MM, Dejong JT (2017) Intersection of modern soil mechanics with ants and roots. Geotech Front 2017:900–909
21. Ghazavi M, Ravanshenas P, El Naggar MH (2013) Interaction between inclined pile groups subjected to harmonic vibrations. Soils Found 53(6):789–803
22. Giannakos S, Gerolymos N, Gazetas G (2012) Cyclic lateral response of piles in dry sand: finite element modeling and validation. Comput Geotech 44:116–131
23. Hazzar L, Hussien MN, Karray M (2017) Numerical investigation of the lateral response of battered pile foundations. Int J Geotech Eng 11(4):376–392. https://doi.org/10.1080/19386362.2016.1224030
24. Hong C-Y, Zhang Y-F, Zhang M-X, Leung LMG, Liu L-Q (2016) Application of FBG sensors for geotechnical health monitoring, a review of sensor design, implementation methods and packaging techniques. Sens Actuators A Phys 244:184–197. https://doi.org/10.1016/j.sna.2016.04.033
25. Ischebeck E, Ischebeck B (2014) Micropile foundations for vertical and horizontal loads-design examples and load test results. In: Proceeding, 12th international workshop on micropiles, international society for micropiles, eighty four, PA, pp 1–20
26. Jewell R, Wroth C (1987) Direct shear tests on reinforced sand. Geotechnique 37(1):53–68
27. Kim BT, Yoon GL (2011) Laboratory modeling of laterally loaded pile groups in sand. KSCE J Civ Eng 15(1):65–75. https://doi.org/10.1007/s12205-011-0924-3
28. Kyung D, Lee J (2018) Interpretative analysis of lateral load–carrying behavior and design model for inclined single and group micropiles. J Geotech Geoenviron Eng 144(1):04017105
29. Lee W, Lee W-J, Lee S-B, Salgado R (2004) Measurement of pile load transfer using the Fiber Bragg Grating sensor system. Can Geotech J 41(6):1222–1232. https://doi.org/10.1139/t04-059
30. Li G-W, Pei H-F, Yin J-H, Lu X-C, Teng J (2014) Monitoring and analysis of PHC pipe piles under hydraulic jacking using FBG sensing technology. Measurement 49:358–367. https://doi.org/10.1016/j.measurement.2013.11.046
31. Lizzi F (1950) First patents on root piles and reticulated root piles, Fondedile, Naples
32. Lu N, Mitchell JK (2019) Geotechnical fundamentals for addressing new world challenges. Springer
33. Lundström T, Jonsson MJ, Kalberer M (2007) The root–soil system of Norway spruce subjected to turning moment: resistance as a function of rotation. Plant Soil 300(1):35–49
34. Martinez A, Dejong J, Akin I, Aleali A, Arson C, Atkinson J, Bandini P, Baser T, Borela R, Boulanger R (2022) Bio-inspired geotechnical engineering: principles, current work, opportunities and challenges. Géotechnique 72(8):687–705
35. Mcaulty J (1956) Thrust loading on piles. J Soil Mech Found Div 82(2):1–25
36. Mcvay M, Casper R, Shang T-I (1995) Lateral response of three-row groups in loose to dense sands at 3D and 5D pile spacing. J Geotech Eng 121(5):436–441. https://doi.org/10.1061/(ASCE)0733-9410(1995)121:5(436)
37. Mcvay MC, Shang T-I, Casper R (1996) Centrifuge testing of fixed-head laterally loaded battered and plumb pile groups in sand. Geotech Test J 19(1):41–50
38. Mcvay M, Zhang L, Molnit T, Lai P (1998) Centrifuge testing of large laterally loaded pile groups in sands. J Geotech Geoenviron Eng 124(10):1016–1026. https://doi.org/10.1061/(ASCE)1090-0241(1998)124:10(1016)
39. Meyerhof G, Ranjan G (1973) The bearing capacity of rigid piles under inclined loads in sand. II: Batter piles. Can Geotech J 10(1):71–85. https://doi.org/10.1139/t73-006
40. Meyerhof G, Sastry V (1985) Bearing capacity of rigid piles under eccentric and inclined loads. Can Geotech J 22(3):267–276. https://doi.org/10.1139/t85-040
41. Monafared S (2012) Numerical study on the behavior of inclined micropiles. Deep Foundations Institute
42. Mondal S, Disfani M, Narsilio GA (2022) Battered minipiles in fine-grained soils: soil-structure interaction. Comput Geotech 147:104762
43. Morrison CS, Reese LC (1988) A lateral-load test of a full-scale pile group in sand, Texas University at Austin Geotechnical Engineering Center
44. Mroueh H, Shahrour I (2009) Numerical analysis of the response of battered piles to inclined pullout loads. Int J Numer Anal Meth Geomech 33(10):1277–1288
45. Othonos A (1999) Fiber bragg gratings. Fundam Appl Telecommun Sens. https://doi.org/10.1063/1.1148392

46. Peck H, Hanson WE (1953) Thornburn, foundation engineering. Wiley, New York
47. Poulos HG, Davis EH (1980) Pile foundation analysis and design. Wiley, New York
48. Randolph M (1980) PIGLET: a computer programme for the analysis and design of pile groups under general loading conditions, Soil Report TR91. Cambridge University
49. Rao SN, Ramakrishna V, Rao MB (1998) Influence of rigidity on laterally loaded pile groups in marine clay. J Geotech Geoenviron Eng 124(6):542–549. https://doi.org/10.1061/(ASCE)1090-0241(1998)124:6(542)
50. Rao SN, Veeresh C (1995) Behaviour of instrumented model batter piles in clays. In: The fifth international offshore and polar engineering conference, 1995. International Society of Offshore and Polar Engineers
51. Rao SN, Veeresh C (1994) Influence of pile inclination on the lateral capacity of batter piles in clays. In: The fourth international offshore and polar engineering conference, 1994. International Society of Offshore and Polar Engineers
52. Reese L, Wang S, Vasquez L (2006) Computer program GROUP Version 7.0—Technical manual, Ensoft Inc, Austin, Tex
53. Richards J, Thomas D, Rothbauer MJ (2004) Lateral loads on pin piles (micropiles), GeoSupport, drilled shafts. Micropil Deep Mix Remed Methods Spec Found Syst 2004:158–174. https://doi.org/10.1061/40713(2004)7
54. Robertson PK (1986) In situ testing and its application to foundation engineering. Can Geotech J 23(4):573–594
55. Robertson PK (2009) Interpretation of cone penetration tests—a unified approach. Can Geotech J 46(11):1337–1355. https://doi.org/10.1139/T09-065
56. Rollins KM, Peterson KT, Weaver TJ (1998) Lateral load behavior of full-scale pile group in clay. J Geotech Geoenviron Eng 124(6):468–478. https://doi.org/10.1061/(ASCE)1090-0241(1998)124:6(468)
57. Sharma B, Hussain Z (2019) Behaviour of batter micropiles subjected to vertical and lateral loading conditions. J Geosci Environ Protect 7(02):206. https://doi.org/10.1080/19386362.2018.1564181
58. Vesic AB (1961) Beams on elastic subgrade and the Winkler's hypothesis. In: 5th ICSMFE, pp 845–850.
59. Walker J, Cox E (1966) Design of pier foundations for lateral loads. Trans ASAE 9(3):417–0420
60. Yen C (1987) Tree root patterns and erosion control. In: Proceedings of the international workshop on soil erosion and its countermeasures. Soil and Water Conservation Society of Thailand, Bangkok, pp 92–111
61. Zhang L, Mcvay M, Han S, Lai P, Gardner R (2002) Effects of dead loads on the lateral response of battered pile groups. Can Geotech J 39(3):561–575. https://doi.org/10.1139/t02-008
62. Zhang L, Mcvay MC, Lai PW (1999) Centrifuge modelling of laterally loaded single battered piles in sands. Can Geotech J 36(6):1074–1084. https://doi.org/10.1139/t99-072
63. Zhang L, Mcvay MC, Lai P (1999) Numerical analysis of laterally loaded 3× 3 to 7× 3 pile groups in sands. J Geotech Geoenviron Eng 125(11):936–946. https://doi.org/10.1061/(ASCE)1090-0241(1999)125:11(936)